

## Temporary Capture of Asteroid Ejecta into Periodic Orbits: Application to JAXA's Hayabusa2 Impact Event

Villegas Pinto, Daniel; Soldini, Stefania; Tsuda, Hiroka; Heiligers, Jeannette

**DOI**

[10.2514/6.2020-0221](https://doi.org/10.2514/6.2020-0221)

**Publication date**

2020

**Document Version**

Accepted author manuscript

**Published in**

AIAA Scitech 2020 Forum

**Citation (APA)**

Villegas Pinto, D., Soldini, S., Tsuda, H., & Heiligers, J. (2020). Temporary Capture of Asteroid Ejecta into Periodic Orbits: Application to JAXA's Hayabusa2 Impact Event. In *AIAA Scitech 2020 Forum: 6-10 January 2020, Orlando, FL* (pp. 1-21). Article AIAA 2020-0221 (AIAA Scitech 2020 Forum; Vol. 1 PartF). American Institute of Aeronautics and Astronautics Inc. (AIAA). <https://doi.org/10.2514/6.2020-0221>

**Important note**

To cite this publication, please use the final published version (if applicable).  
Please check the document version above.

**Copyright**

Other than for strictly personal use, it is not permitted to download, forward or distribute the text or part of it, without the consent of the author(s) and/or copyright holder(s), unless the work is under an open content license such as Creative Commons.

**Takedown policy**

Please contact us and provide details if you believe this document breaches copyrights.  
We will remove access to the work immediately and investigate your claim.

# Temporary Capture of Asteroid Ejecta into Periodic Orbits: Application to JAXA’s Hayabusa2 Impact Event

Daniel Villegas Pinto<sup>\*</sup>, Stefania Soldini<sup>†</sup>, Yuichi Tsuda<sup>‡</sup>, Jeannette Heiligers<sup>§</sup>

**In this paper, we study the dynamical environment around asteroids to investigate whether ejecta particles from an impact event (artificial or natural) could be temporarily trapped in periodic orbits. If such particles remain about an asteroid, they could potentially jeopardize an orbiting spacecraft in the event of a collision. We make use of invariant manifold theory to assess the conditions - impact location, particle radius, ejection velocity - that cause ejecta particles to get captured in periodic orbits. The analysis is carried out within the dynamical framework of the perturbed Augmented Hill Problem, which takes into account the solar radiation pressure, the effect of eclipses, and the  $J_{20}$  and  $J_{40}$  terms of the asteroid’s gravity potential in its spherical harmonics expansion. We analyze millimeter- to centimeter-sized particles and captures into three families of periodic orbits that are robust to large values of the solar radiation pressure acceleration – the traditional  $a$  and  $g'$  families of the Hill Problem and the southern halo orbits. We go on to find the impact locations from where ejecta particles are most likely to be captured into periodic orbits via their stable manifolds. As such, we recover the sets of initial states that lead ejecta to temporary orbital capture and show that solar radiation pressure and, subsequently, eclipses, cannot be neglected in these analyses. We apply our analyses to the specific case of JAXA’s Hayabusa2 mission that successfully carried out its Small Carry-on Impactor (SCI) operation at asteroid Ryugu in April 2019. For this event, we identify locations on the Sun side of the asteroid at medium latitudes as the best impact locations.**

## I. Introduction

After having arrived at asteroid Ryugu at the end of June 2018, JAXA’s Hayabusa2 completed its Small-Carry-on-Impactor (SCI) operation in April 2019. The operation consisted of firing a kinetic impactor at the asteroid with the purpose of later collecting subsurface material from the created crater via a final touchdown [1]. Hayabusa2 is not the only mission that has planned a kinetic impact on an asteroid: the joint ESA/NASA AIDA mission intends to impact the moon of the binary asteroid Didymos, in an effort to study asteroid deflection [2]. Observations of asteroid P/2010 A2 (seen to have a debris trail, likely resultant of a collision) [3] and other studies [4] have shown the possibility of dust particles remaining about the asteroid for long periods of time as a product of an impact event. Due to the small mass of most asteroids, the dynamical environment of the ejecta is highly perturbed by solar radiation pressure (SRP). Although these conditions are often disruptive to the possibility of bounded motion, they may give rise to scenarios that result in temporary capture, posing a danger to missions in the case of collision with a spacecraft. Moreover, temporary capture of ejecta particles about asteroids could prevent spacecraft from approaching the asteroid for follow-up operations, as is the case with Hayabusa2’s final sample collection of the material excavated by the SCI. This is thus the motivation for the undertaking of this work; its purpose is to assess the conditions that could cause ejecta to remain captured in periodic orbits about an asteroid following an impact event on its surface. Taking advantage of Hayabusa2’s SCI operation, we apply this analysis to the specific case of asteroid Ryugu for a study on ejecta dynamics.

The dynamical environment presented here is, at its core, based on the Hill Problem [4–6]. However, the classical Hill Problem does not include the effect of the SRP, which is a major perturbation of the system under consideration [7, 8]. Also known as the Photogravitational Hill Problem [9], the extension of the Hill Problem to the case of a radiating primary is here referred to as the Augmented Hill Problem (AHP). The model used in this paper is a further extension of the AHP, here referred to as the perturbed AHP, which also includes the effect of eclipses and the asteroid’s  $J_{20}$  and  $J_{40}$  terms of its spherical harmonics gravity potential expansion.

---

<sup>\*</sup>Delft University of Technology, Delft, The Netherlands, daniel.villegas-pinto@obspm.fr. Currently at IMCCE/Paris Observatory, Paris, France

<sup>†</sup>ISAS/JAXA, Sagami-hara, Kanagawa, Japan. Currently at the University of Liverpool, Liverpool, UK

<sup>‡</sup>ISAS/JAXA, Sagami-hara, Kanagawa, Japan

<sup>§</sup>Delft University of Technology, Delft, The Netherlands

Several orbital dynamics studies have been carried out under the AHP model. In [9], an extensive search and analysis of families of planar periodic orbits is undertaken for very small values of SRP acceleration. The AHP has also been used to study the dynamics of solar sails about asteroids, as seen in [10, 11]. In [12], Broschart and Villac explore an orbit family previously presented in [13–15], known as the terminator family (the equivalent of the southern halo orbits in the CR3BP [16]), which is shown to exhibit long-term stability in heavily SRP-perturbed environments and robustness against gravitational uncertainties. This type of orbit and its quasi-periodic family branches are further analyzed in [17]. Also of interest are the works presented in [18] and [19], where families of periodic orbits for large values of SRP acceleration are analyzed. Specifically, in [18], various families of three-dimensional symmetric periodic orbits are presented as orbiting possibilities for Hayabusa2 about asteroid Ryugu. In [19], planar orbit families of the Hill Problem are continued into and analyzed in the AHP up to very high values of SRP. The work in [19] also presents the effect of eclipses on the family-parameter curve and the shape of these orbit families, which proves especially relevant when considering large values of SRP acceleration and is further explored in this paper.

In [7], Scheeres et al. present an extensive review on the types of trajectories ejecta particles can take after being lofted from an asteroid’s surface, which perturbations should be taken into account, and possibilities regarding the modeling of these trajectories and particles. They present basic dynamical equations and models, and a classification scheme for the possible fate of the ejecta particles. In [20], the dynamics of ejecta particles in close-proximity of asteroid 4769 Castalia are studied extensively using a radar-derived shape model. Although the model considers only the asteroid’s gravity, ranges of velocities that guarantee either re-impact or escape are obtained and remarks relating to capture conditions are addressed. Scheeres and Marzari [4] simulate extensive sets of initial conditions via an analytical method to find those that cause dust particles to be temporarily trapped about comet 9P/Tempel after ejection from its surface. Finally, Soldini and Tsuda [21] study the fate of asteroid ejecta about asteroid Ryugu by simulating different initial conditions and integrating them forwards in time, both in the two-body problem and the AHP, leading to conclusions on the fact that smaller particles (large values of SRP acceleration) are likely to escape or re-impact faster.

All these works form a basis for the general understanding that (quasi)-periodic orbits can exist in the heavily-perturbed orbital environment about NEOs. The problem investigated in this paper builds on these works by investigating the sets of initial conditions that enable millimeter- to centimeter-sized asteroid ejecta to get captured into periodic orbits and consequently pose a danger to the Hayabusa2 spacecraft. In this paper, these initial conditions are found by making use of the stable invariant manifolds of periodic orbits, to find trajectories that lead from the asteroid surface to said orbits. The proposed method departs from the more common approach of simulating wide ranges of initial conditions to find the ones that lead to temporary captured motion – as done in [4, 21] –, thus closing the knowledge gap on specific conditions that lead to temporary capture into periodic orbits.

This paper is structured as follows. We first introduce the dynamical models and equations of motion used in Section II, presenting the AHP model, eclipse model, and gravity model that includes the asteroid’s  $J_{20}$  and  $J_{40}$  terms of the body’s gravity potential spherical harmonics expansion – here referred to as  $J_2$ ,  $J_4$  for conciseness. Following this, the methodology is presented regarding periodic orbits and their study in the different models in Section III. We then detail the used approach in Section IV, with its assumptions and considerations, thus linking the theoretical background with its practical applications. This is followed in Section V by the presentation of the results for the planar and three-dimensional cases, the implications of said results for the Hayabusa2 mission and, finally, the conclusions of the work.

## II. Dynamical Model

This section presents the models and theoretical background used throughout this work. The asteroid is assumed to be on a circular orbit about the Sun with constant mean motion  $\omega$ , and is initially modeled as a point mass for the AHP and the eclipse models. Later, the  $J_2$  and  $J_4$  (i.e., the  $C_{20}$  and  $C_{40}$  Stokes coefficients) gravitational terms are implemented. Other forces such as electromagnetic forces, the Poynting-Robertson effect, or the Yarkovsky effect are neglected due to their very small intensity and the fact they only act on very long time scales [22]. Moreover, we neglect collisions between particles.

A rotating reference frame is adopted,  $\mathbf{R}_1(\hat{x}_{Hill}, \hat{y}_{Hill}, \hat{z}_{Hill})$ , hereon referenced as the Hill frame. The Hill frame is centered in the center of mass of the asteroid, its  $x_{Hill}$ -axis points in the anti-solar direction at all times, its  $z_{Hill}$ -axis points in the direction of the asteroid’s orbit angular momentum vector, and the  $y_{Hill}$ -axis completes the orthogonal frame.

### A. The Augmented Hill Problem

The AHP and Hill Problem are derived from the Circular Restricted Three-Body Problem (CR3BP), by approximating the dynamics to the vicinity of the secondary body, in this case the asteroid [6, 23]. Following [4, 8], the equations of motion are normalized using as unit of length  $[l] = (\mu/\omega^2)^{1/3}$  and as unit of time  $[t] = 1/\omega$ , where  $\mu$  is the asteroid's gravitational parameter. They take the form (omitting the subscript "Hill" from hereon in equations)

$$\ddot{x} - 2\dot{y} = -\frac{x}{r^3} + 3x + \beta \quad (1)$$

$$\ddot{y} + 2\dot{x} = -\frac{y}{r^3} \quad (2)$$

$$\ddot{z} = -\frac{z}{r^3} - z \quad (3)$$

where  $r = \sqrt{x^2 + y^2 + z^2}$  and  $\beta$  is the non-dimensional SRP acceleration.

The SRP is assumed to be constant and acting along the Sun-asteroid direction. The non-dimensional SRP acceleration,  $\beta$ , is then obtained by normalizing the traditional SRP acceleration,  $a_{SRP}$ , for a cannonball model [8, 17, 24], i.e., with a constant exposed area and attitude, which yields

$$\beta = \frac{a_{SRP}}{[l]/[t]^2} = \frac{(1 + C_R)P_0}{m/A \mu^{1/3} \mu_S^{2/3}} \quad (4)$$

where  $C_R$  is the reflectivity coefficient or albedo,  $P_0 \approx 1.02 \times 10^{17} \text{ kg m s}^{-2}$  is the solar constant,  $m/A$  is the mass-to-area ratio, and  $\mu_S$  is the gravitational parameter of the Sun.

The system presented in Eqs. (1)-(3) admits an energy integral,  $C$ , known as the Jacobi Constant [8]

$$C = 2\tilde{U} - V^2 = 3x^2 + 2\beta x + \frac{2}{r} - z^2 - (\dot{x}^2 + \dot{y}^2 + \dot{z}^2) \quad (5)$$

where  $\tilde{U} = \frac{3}{2}x^2 + \beta x + \frac{1}{r} - \frac{z^2}{2}$  and  $V = \sqrt{\dot{x}^2 + \dot{y}^2 + \dot{z}^2}$  represent, respectively, the effective potential and kinetic energies of the system [8]. Since  $V \geq 0$ , We can write  $V^2 = 2\tilde{U} - C \geq 0$ , which translates into the regions of accessible and forbidden motion of a particle, and whose boundaries are the Zero-Velocity Curves (ZVC) [23].

By setting the left-hand side of Eqs. (1)-(3) to zero, we find the Lagrangian equilibrium points of the system. Contrary to the traditional CR3BP, the system admits only two equilibrium points,  $L_1$  and  $L_2$ , both of them on the  $x$ -axis. The equilibrium point  $L_1$  lies along the negative  $x$ -axis, i.e., on the asteroid's Sun side, and  $L_2$  along the positive side of the  $x$ -axis. An increase in SRP acceleration causes the  $L_1$  point to move towards the Sun and the  $L_2$  point to asymptotically move towards the asteroid. For this reason, the  $L_1$  point loses its significance to our analysis, as it is too far from the asteroid. In this paper, we consider ejecta particles from millimeter to centimeter sizes, which in turn translate into a large range of  $\beta$ -values.

**Table 1 Asteroid Ryugu Properties [21, 25]**

$\mu$ [ $\text{m}^3 \text{s}^{-2}$ ]	Asteroid axes [m]			Avg. radius, $R_a$ [m]	Orb. period, $T_a$ [days]	Density, $\rho$ [ $\text{kg}/\text{m}^3$ ]	$C_R$
	a	b	c				
32	446.5	439.7	433.9	440	473.889287	1270	0.07

The ejecta particles are modeled as spheres of constant density and have material characteristics equal to those of asteroid Ryugu, i.e., same density,  $\rho$ , and reflectivity,  $C_R$ . The properties of asteroid Ryugu are shown in Table 1. Table 2 shows the relation between different values of  $\beta$ , radius, mass-to-area ratio,  $a_{SRP}$ , and the  $x$  coordinate of the  $L_2$  point,  $x_{L_2}$ , together with its corresponding Jacobi constant,  $C_{L_2}$ . Note that even for a spacecraft, the SRP acceleration values about Ryugu are significant. For instance, Hayabusa2's non-dimensional SRP acceleration is situated between  $\beta = 40$  and  $\beta = 50$ , for a mass-to-area ratio of  $35 \text{ kg}/\text{m}^2$  [18] and an albedo of 0.3. Finally, in order to analyze millimeter- to centimeter-sized particles, we focus on  $\beta$ -values ranging between  $\beta = 30$  and  $\beta = 200$  for the remainder of this paper, highlighted in Table 2.

**Table 2 Relationship between non-dimensional SRP acceleration ( $\beta$ ), mass-to-area ratio ( $m/A$ ), particle radius ( $R$ ), dimensional SRP acceleration ( $a_{SRP}$ ), Jacobi constant of the  $L_2$  point ( $C_{L_2}$ ), and position of the  $L_2$  point ( $x_{L_2}$ ).**

$\beta$	$\frac{m}{A}$	$R$ [cm]	$a_{SRP}$ [mm/s <sup>2</sup> ]	$C_{L_2}$ [-]	$x_{L_2}$ [km]
0	-	-	0	4.327	76.8
10.0	132.2	15.61	$2.608 \times 10^{-5}$	12.94	33.54
30.0	44.06	5.204	$7.825 \times 10^{-5}$	22.01	20.04
50.0	26.44	3.123	$1.304 \times 10^{-4}$	28.34	15.6
100.0	13.22	1.561	$2.608 \times 10^{-4}$	40.03	11.06
200.0	6.61	0.7807	$5.217 \times 10^{-4}$	56.58	7.828
300.0	4.406	0.5204	$7.825 \times 10^{-4}$	69.29	6.393

## B. Eclipse Model

Given the magnitudes of SRP accelerations considered, eclipses are likely to pose a significant perturbation to the particles whose trajectories cross the eclipse region. To model this perturbation, a cylindrical eclipse model is adopted. The transition between the eclipse and sunlit regions are simulated by means of a modified sigmoid function (smooth step function) [26] of the form  $g(\chi) = (1 + e^{-s\chi})^{-1}$ , where  $\chi$  is the input and  $s > 0$  is often referred to as the contrast factor term (where we use  $s = 8$ ), which defines the steepness and "length" of the transition. Using this function, we can redefine the value for the SRP acceleration,  $\beta^*$ , as

$$\beta^* = \begin{cases} \beta & \text{if } x \leq 0 \\ \beta g(r_{sig}) & \text{otherwise} \end{cases} \quad (6)$$

where  $r_{sig} = (r_x - R_a)$ , and  $r_x$  is the distance to the  $x$ -axis,  $r_x = \sqrt{y^2 + z^2}$ .

## C. Gravity Perturbations

To better represent the physical environment experienced by ejecta particles around asteroid Ryugu, a higher-fidelity representation of the asteroid's gravity is presented by considering the  $J_2$  and  $J_4$  terms of its spherical harmonics expansion. The common notation  $J_2 = -C_{20}$  and  $J_4 = -C_{40}$  is used, where  $C_{lk}$  refers to the term of the Stokes coefficients with degree  $l$  and order  $k$ .

Data from the Hayabusa2 team have shown that asteroid Ryugu's spin-axis is oriented approximately normal to its orbital plane. Since it spins about its shortest axis,  $c$ , i.e., the axis with largest moment of inertia [8], we can include the gravity perturbations of the  $J_2$  and  $J_4$  terms without affecting the existing dynamical symmetry of the system with respect to the  $xz$ -plane [13]. Note that since we consider only the Stokes coefficients with order zero (and degrees two and four), we can use the Hill frame to define the gravity potential of the asteroid, and do not need to perform the usual reference frame transformation from the body-fixed frame to the rotating Hill frame. The non-dimensional gravity potential in its spherical harmonics expansion then becomes [27]

$$U(r, \delta) = \frac{1}{r} \left[ 1 + \left(\frac{r_0}{r}\right)^2 \left(\frac{1}{2}C_{20} (3 \sin^2 \delta - 1)\right) + \left(\frac{r_0}{r}\right)^4 \left(\frac{1}{8}C_{40} (35 \sin^4 \delta - 30 \sin^2 \delta + 3)\right) \right] \quad (7)$$

where  $\delta$  is the particle's declination in the Hill frame. Expressing  $r$  and  $\delta$  in Cartesian coordinates and differentiating with respect to  $x$ ,  $y$ , and  $z$ , we can derive the accelerations in the respective directions, i.e.,  $U_x, U_y, U_z$ .

Finally, as a concluding remark regarding the incorporation of the different perturbations considered for the model in this paper, we analyze the magnitudes of the various perturbing accelerations,  $a_p$ , to a particle about asteroid Ryugu. Figure 1 shows the dimensional accelerations of the different perturbing sources along the  $x$ -axis, where we also include the Sphere of Influence (SOI) of the asteroid,  $R_{SOI} = d_a(\mu/\mu_S)^{2/5}$  [28], where  $d_a = 1.189558056$  AU is the mean distance from the Sun to the asteroid, calculated from  $T_a$  and assuming a circular orbit. As expected, the gravitational acceleration is the main perturbation when in close-proximity to the asteroid; however, just outside the SOI, the magnitudes of the SRP accelerations are of the same order of magnitude as the asteroid's gravity acceleration, and actually become larger for distances larger than 12 km for  $\beta = 200$  ( $R = 7.8$  mm) and larger than 20 km for  $\beta = 30$  ( $R = 5.2$  cm).

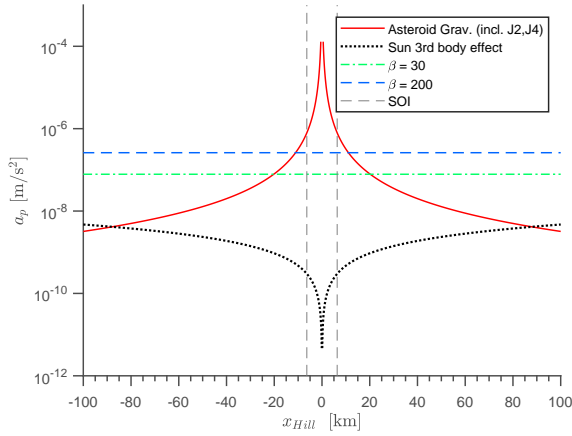


**Fig. 1** Magnitude of the perturbing accelerations about Asteroid Ryugu as a function of the  $x$ -coordinate.

### III. Periodic Orbits

This section presents the methodology used in this work, related to the computation and analysis of periodic orbits. The orbit families studied in this paper are also presented and analyzed in terms of stability, geometry, and the effects of the different perturbations to the system.

#### A. Symmetries and Stability

The system presented in the previous section displays the following symmetries [29]

$$(y, t) \rightarrow (-y, -t) \quad (8)$$

$$(y, z, t) \rightarrow (-y, -z, -t) \quad (9)$$

$$(z) \rightarrow (-z) \quad (10)$$

From Eqs. (8)-(10), we can conclude that if a trajectory satisfies  $(y, \dot{x}, \dot{z}) = 0$  or  $(y, z, \dot{x}) = 0$  at two different times  $t_1 \neq t_2$ , the resulting orbit will be periodic. This condition is used to find periodic orbits via differential correction [30]. Once a periodic orbit is found, a family continuation algorithm is adopted, which makes use of a modified version of the pseudo-arclength continuation method [31]. Both these methods make use of the State Transition Matrix (STM) of the system [32],  $\Phi(t, t_0)$ , which is integrated alongside the equations of motion.

When studying periodic orbits, the STM can be analyzed after one period,  $T$ , (then known as the Monodromy Matrix,  $\Phi_M = \Phi(T, t_0)$ ) to provide information about the orbit's stability. The eigenvalues of the Monodromy matrix occur in three reciprocal pairs [16], as  $\{\lambda_1, \frac{1}{\lambda_1}, \lambda_2, \frac{1}{\lambda_2}, 1, 1\}$ . The two unit pairs are a characteristic of the energy integral of the system and are always situated on the unit circle. A periodic orbit will be stable if all its eigenvalues are situated on the unit circle. Introducing the following stability indices  $k_1, k_2$  [16]

$$k_i = \lambda_i + \frac{1}{\lambda_i} \quad (11)$$

an orbit will be stable if  $|k_i| < 2$  and  $k_i$  is real for  $i = 1, 2$ .

#### B. Periodic orbits of the AHP and perturbed AHP models

##### 1. AHP model

In the traditional Hill Problem studied by Hénon in [6], five families of periodic orbits are identified:  $a, g, g', f$ , and  $c$ . The  $a$  and  $c$  families correspond to planar Lyapunov orbits about the  $L_2$  and  $L_1$  points, respectively; the  $g$  and  $f$  families correspond to Distant Prograde Orbits (DPOs) and Distant Retrograde Orbits (DROs), respectively; and family  $g'$  corresponds to a bifurcation from the  $g$  family. In [19], the effect of SRP on these families is presented, showing that the  $g$  family crosses the origin of the reference frame for increasing values of SRP acceleration; families  $c$  and  $f$  lose their significance to our problem as they move with the  $L_1$  point towards the Sun; and families  $a$  and  $g'$  get closer to the

asteroid with the  $L_2$  point. For these reasons, we focus on the  $a$  and  $g'$  families, which can be seen in Figures 2 and 3 for different values of  $\beta$ . Additionally, regarding their stability, while the doubly-periodic family  $g'$  is unstable in the Hill Problem [6], the addition of the SRP acceleration stabilizes the family [19]. Family  $a$ , however, is unstable in both the traditional Hill Problem and the AHP, for all values of SRP accelerations considered.

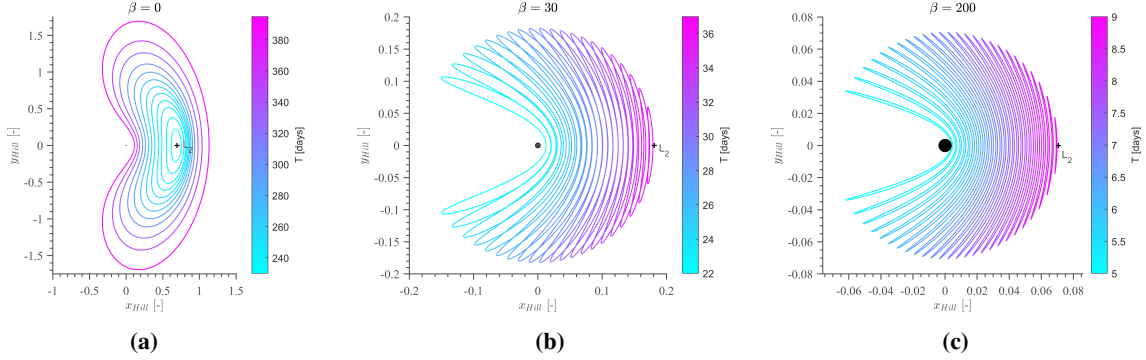


**Fig. 2** Family  $a$  of planar Lyapunov orbits in the AHP model for different values of SRP acceleration.

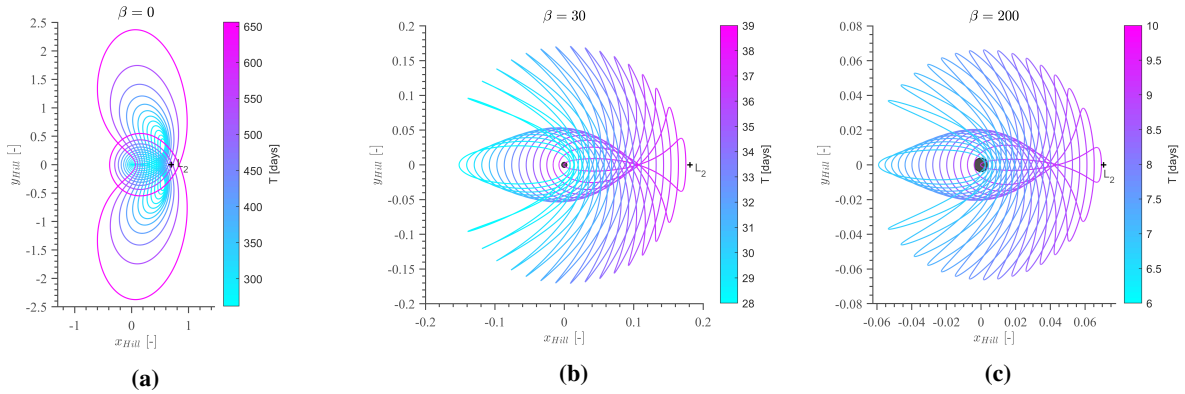


**Fig. 3** Family  $g'$  in the AHP model for different values of SRP acceleration.

The third and final family of periodic orbits analyzed in this work is the family of southern halo orbits, which are commonly known as terminator orbits in the AHP [8, 12, 17] due to their existence close to the Sun-terminator plane, i.e., the plane through the asteroid's center of mass perpendicular to the Sun-asteroid line. Figure 4 shows the family of terminator orbits, showing that the family approaches the terminator plane for increasing  $\beta$ -values. However, it does not show significant changes to its geometry. A portion of the terminator orbit families is always stable; in fact, this region increases when including SRP.

The choice for studying the planar  $a$  and  $g'$  families arises from the natural evolution of the planar families with the inclusion of the SRP acceleration. In addition, and specifically for the Hayabusa2 case, both the spacecraft and the planned impact location were placed close to the ecliptic plane. The choice for studying terminator/halo orbits for the three-dimensional case arises from their previously studied characteristics, which hint at the possibility of presenting a potential hazard to spacecraft: terminator orbits have been noted to be robust to very large values of SRP acceleration and uncertainties in the gravitational model [12, 17, 33]. A final reason for studying both the terminator orbits and planar Lyapunov orbits (family  $a$ ) is that they originate from the  $L_2$  equilibrium point, which acts as a gateway for re-impacting, orbiting, and escaping trajectories in the AHP. The analysis of the collinear equilibrium point orbits can therefore provide insight into the possibility of escape versus re-impact of the ejecta particles.

## 2. AHP + Eclipse model

Terminator orbits are largely unaffected by eclipses, except close to the bifurcation with family  $a$  near the  $L_2$  point. For simplicity we neglect these few orbits of the terminator family. On the contrary, families  $a$  and  $g'$  always cross the

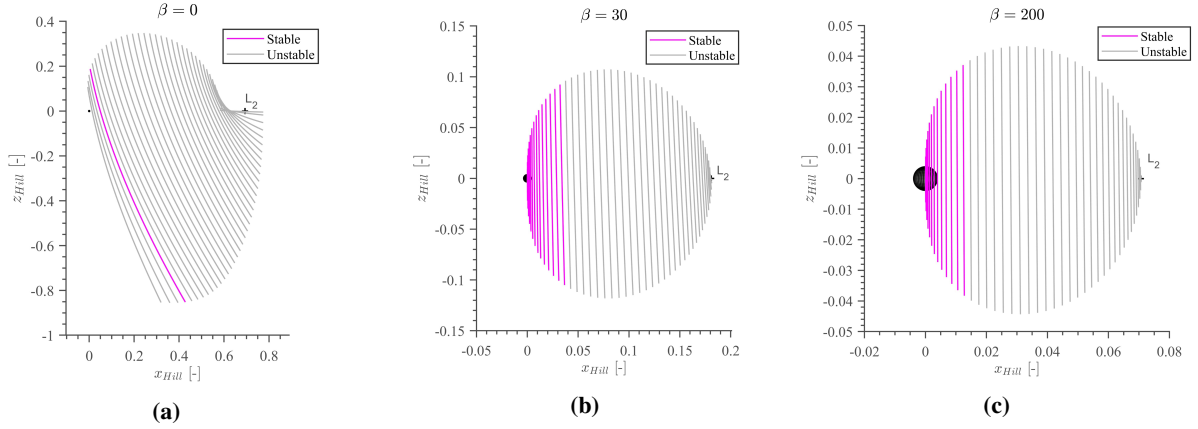


**Fig. 4 Family of terminator orbits for different values of SRP acceleration.**

eclipse region, which implies that their periodic solutions in the eclipse model are required for their analysis.

The inclusion of eclipses creates an implicit time dependence, causing the SRP acceleration and in turn the energy integral portrayed in Eq. (5) to vary. However, for an orbit to be periodic, so must this variation, in order to maintain the standard condition of periodicity  $X(t) = X(t + T)$  [23], where  $X = [x, y, z, \dot{x}, \dot{y}, \dot{z}]^T$ . Moreover, as the symmetry conditions in Eqs. (8)-(10) are maintained when including eclipses, periodic solutions will still exist in the system.

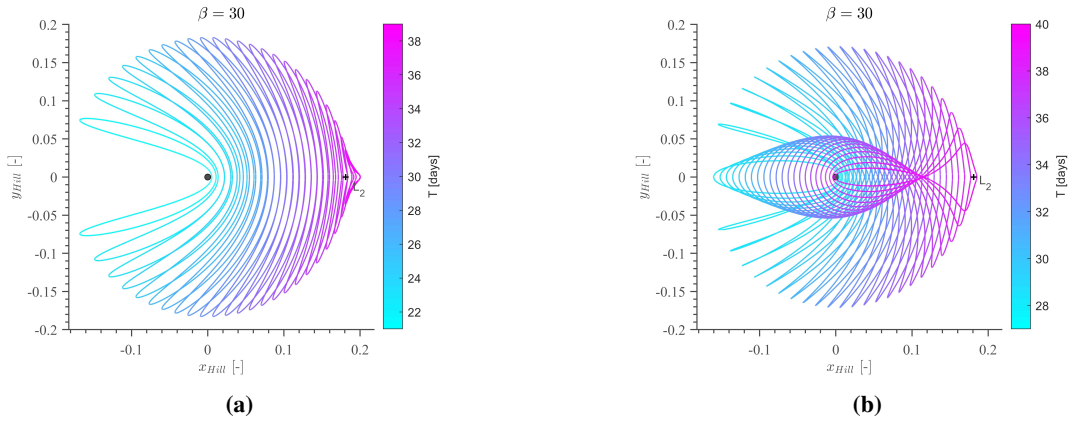
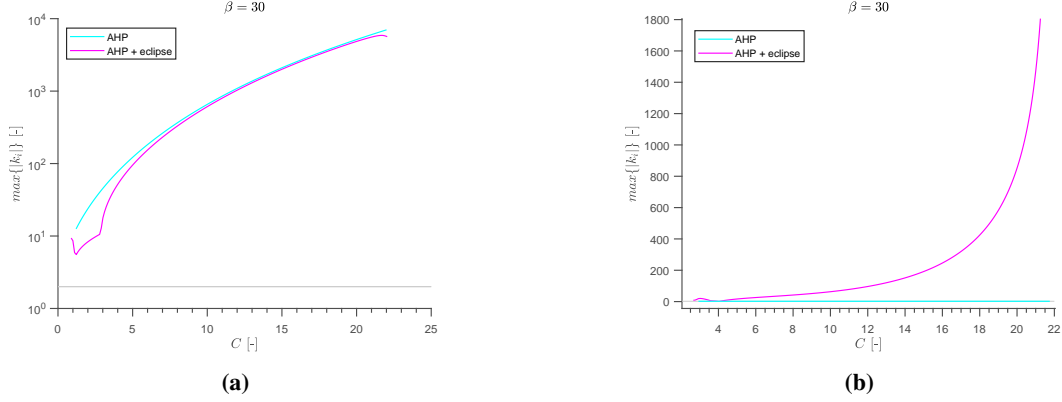


**Fig. 5 (a) Family  $a$  and (b) family  $g'$  in the AHP + eclipse model for  $\beta = 30$ .**

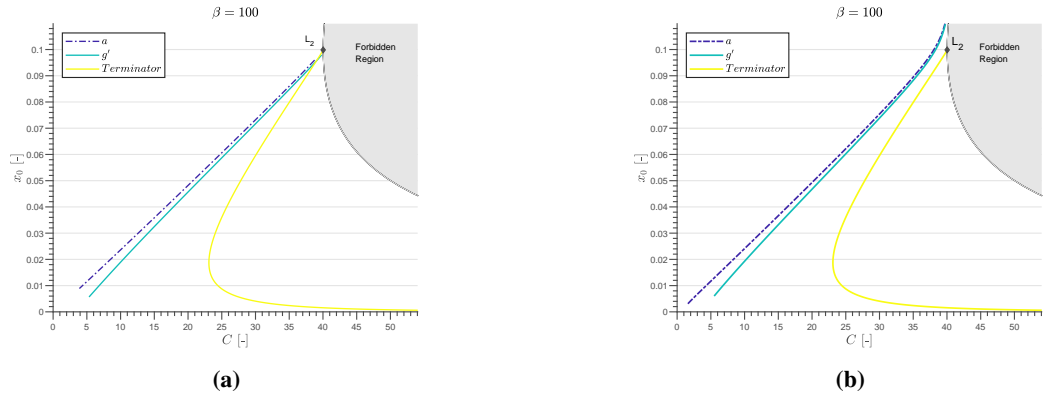
From Figure 5 we can see how the geometry of families  $a$  and  $g'$  changes in the AHP + eclipse model. Specifically, we can see that the families continue past the  $L_2$  equilibrium point. Given there is no SRP acceleration in the eclipse region, the equilibrium point will actually take its position for  $\beta = 0$ , which allows the orbits in the AHP + eclipse model to extend past the  $L_2$  point. The inclusion of eclipses also has implications on the regions of accessible motion defined by the ZVCs. Due to the periodic variation of the Jacobi constant, these regions will not be constant along the orbit but rather vary periodically.

Figure 6 shows the effect of eclipses on the stability of the  $a$  and  $g'$  families. We see that the eclipses not only affect the geometry of the orbits but also their stability. Family  $g'$  becomes unstable for all values of  $\beta$ , while family  $a$  becomes slightly more stable with increasing values of  $\beta$ . For the general case, this change in stability will only occur when SRP plays a significant role in the dynamics, which is the case when studying the dynamics about small bodies (see Figure 1), even for spacecraft [33]. Note that in Figure 6, and whenever referring to the Jacobi constant in the AHP + eclipse model, we take the value of the nominal Jacobi constant, i.e., ignoring the variation due to eclipses. Although the variation of the Jacobi constant between the eclipse and non-eclipse regions can be significant (an order of magnitude), a particle only spends a very small part of the orbit in eclipse (less than 2% of the period).

Figure 7 shows the family curves in terms of the initial  $x$  coordinate and the Jacobi constant of the  $a$ ,  $g'$ , and



**Fig. 6** Stability of (a) family  $a$  and (b) family  $g'$  in the AHP and AHP + eclipse models for  $\beta = 30$ .



**Fig. 7** Family curves of the  $a$ ,  $g'$ , and terminator families in the (a) AHP model and (b) in the AHP + eclipse model, for  $\beta = 100$ .

terminator families in both the AHP and the AHP + eclipse models. Comparing Figures 7a and 7b, we see once again how the  $a$  and  $g'$  families extend past the  $L_2$  point due to the inclusion of eclipses.

### 3. Perturbed AHP model

Because the perturbation posed by the  $J_2$  and  $J_4$  terms is very small when compared to the other perturbations, the shape of the orbits does not change significantly when we include them in the model. From Eq. (7), we see that the gravity potential decreases by powers of  $r^2$  and  $r^4$ , which means that the effect of these perturbations will only be significant in close-proximity to the asteroid. Therefore, the inclusion of the  $J_2$  and  $J_4$  terms will affect the trajectories in those regions, which, considering that the particles are ejected from the asteroid surface, can be significant. Finally, the change in stability to the  $a$ ,  $g'$ , and terminator families is almost negligible when adding the gravity perturbations.

## IV. Particle Ejection Dynamics

In this section we discuss the considerations surrounding the ejection of particles from the asteroid and how we can study the particles that are captured in periodic orbits.

### A. Ejection angle

Previous work has considered the problem of asteroid ejecta as a product of a ballistic impact [34, 35]. While more research regarding the ejection angle and velocity distribution for different impact angles, velocities, and surface materials is surely necessary, it is common to assume an ejection angle close to  $45^\circ$  with the surface normal [34, 36]. This assumption is based on existing literature and experiments, which show that for impact angles smaller than  $60^\circ$  with respect to the surface normal, the ejection angles tend to exist between  $35^\circ$  and  $50^\circ$  from the surface normal for

non-high-velocity particles [37, 38]. Only for very oblique angles have the non-high-velocity particles shown to deviate from this ejection direction and have craters shown more evident asymmetry [39, 40]. In this paper, we assume the impact angle to be smaller than  $60^\circ$  with respect to the surface normal. This assumption holds true also for the case of Hayabusa2’s SCI, given that its impact angle error relative to three-standard deviations (99.7%) corresponded to an error of approximately  $26^\circ$  from the surface normal [41], far smaller than  $60^\circ$ . Note that when considering the high- or hyper-velocity ejecta particles, this ejection direction may not be observed [42], but given that said particles have far larger velocities than the escape velocity of the asteroid, and will therefore not be captured, the assumption is still valid for our study. For these reasons, we assume the regolith particles to be ejected only within the range  $\sigma \in [35^\circ, 50^\circ]$ , where  $\sigma$  is the ejection angle with respect to the surface normal.

## B. Invariant Manifolds and Particle Ejection

In order to identify a link between a particle being ejected from the asteroid surface and the periodic orbits, we make use of invariant manifold theory, calculating the unstable invariant manifolds of trajectories that would arrive at the analyzed periodic orbits [43]. Figure 8 shows the stable and unstable manifolds of a planar Lyapunov orbit (family  $a$ ) for  $\beta = 0$ , while Figure 9 shows the stable manifolds for the same family but for different values of  $\beta$  in the AHP model. Both figures present also the regions of forbidden motion defined by the ZVCs. Note how the shape of the manifolds approach the shape of the ZVCs for increasing values of  $\beta$ . Since we want to study the motion of particles arriving at the orbits as opposed to those departing from them, we focus only on the stable manifolds of periodic orbits.

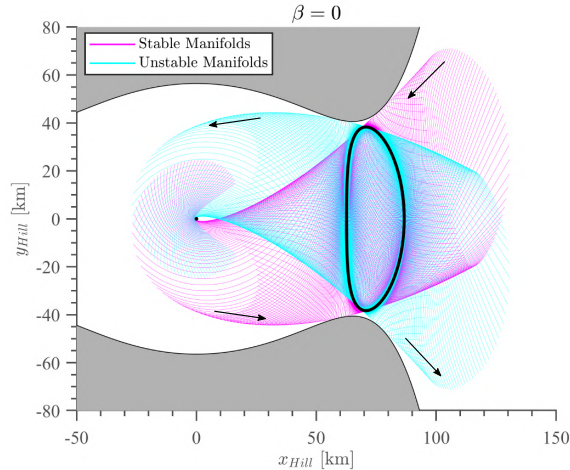


**Fig. 8** Stable and unstable invariant manifolds of an orbit from family  $a$  for  $\beta = 0$ . The region of forbidden motion defined by the ZVC is shown in gray.

Besides computing the invariant manifolds of periodic orbits, we can also compute the invariant manifolds of the equilibrium points, as mapping the structure of their manifolds may provide insight into the fundamental motion of the particles. The interior stable manifolds of the  $L_2$  point in the AHP model for different values of  $\beta$  are shown in Figure 10. Note that for larger values of  $\beta$ , the stable manifolds of  $L_2$  intersect with the asteroid surface.

Comparing Figures 8, 9, and 10, we can see how the general direction and shape of the manifolds of family  $a$  follows the structure of the manifolds of  $L_2$ . As  $\beta$  increases, the manifolds tend to travel closer along the  $x$ -axis, intersect with the asteroid, and become more symmetric with respect to the  $x$ -axis. Moreover, as the nominal orbits approach the  $L_2$  point, their stable manifolds mimic those from the equilibrium point. This is explained by the fact that family  $a$  (as well as the terminator family), originate from  $L_2$ .

## C. Trajectory simulation

To find the initial conditions and trajectories that cause the ejecta particles to be temporarily trapped in the considered periodic orbits, we divide each orbit in 250 equidistant nodes, perturb the state of each in the direction of its local stable eigenvector, and integrate backwards in time. The integration is carried out until one of three stopping conditions is met: (1) escape from the system; (2) impact with the asteroid; (3) total integration time reaches 150 days. Note that we

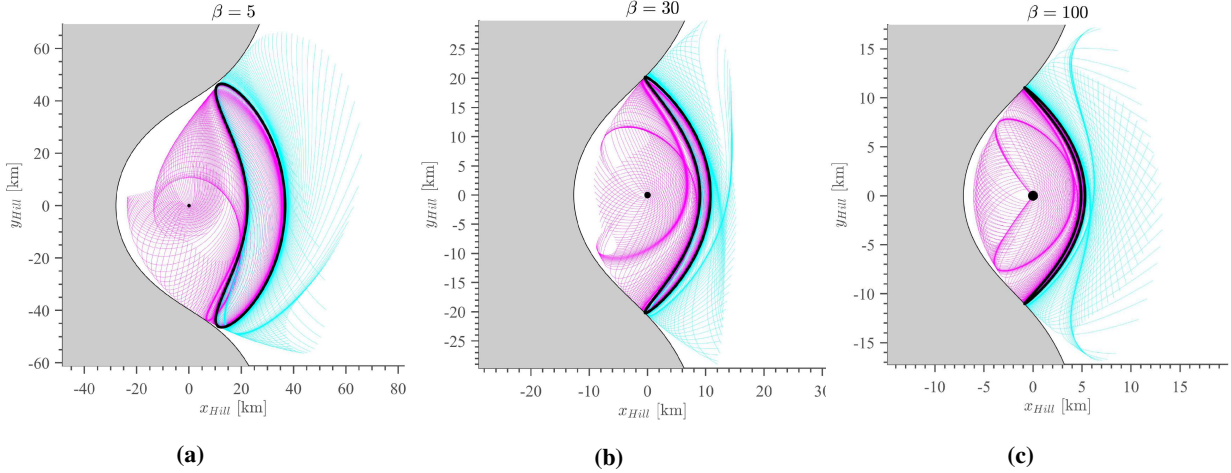


**Fig. 9** Stable manifolds for orbits of family *a* in the AHP model for different values of the SRP acceleration. Interior manifolds are shown in pink and exterior manifolds in blue. The regions of forbidden motion defined by the ZVCs are shown in gray.

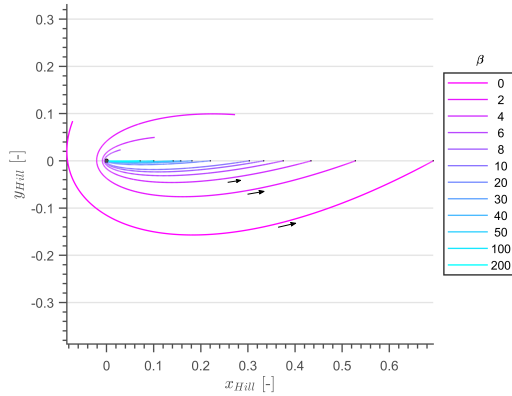


**Fig. 10** Interior stable manifolds of the  $L_2$  equilibrium point for different values of SRP acceleration.

consider the "impact" radius to be slightly larger than the largest axis of the asteroid, to avoid entering the Brillouin sphere of the gravity's spherical harmonics [8]. The simulations are carried out in the full model, including eclipses and gravity perturbations. We consider SRP acceleration values of  $\beta = \{30, 40, 50, 75, 100, 125, 150, 175, 200\}$ , which correspond, respectively, to ejecta particle radii of  $R \approx \{5.2, 3.9, 3.1, 2.1, 1.6, 1.2, 1.0, 0.9, 0.8\}$  cm. For each  $\beta$ /radius pair and family of periodic orbits described, we select equidistant orbits along the family, selecting at least 200 orbits per family. By selecting a large number of equidistant orbits along each family we aim to sample the characteristics and structure of said family for each value of  $\beta$ , and thus obtain representative results for the dynamical environment about the asteroid.

To facilitate the presentation of the results shown in future sections, we establish the following spherical coordinates, defined in the Hill frame: the right ascension,  $\zeta$ , which is the angle measured in the  $xy$ -plane from the  $x$ -axis in a positive direction; and the declination,  $\delta$ , measured from  $xy$ -plane in the direction of the  $z$ -axis, shown in Figure 11.

## V. Results

This section presents the results obtained from the invariant manifolds analysis described in the previous sections. All results are obtained using the full model, which considers SRP, eclipses, and the gravity perturbations of the  $J_2$  and  $J_4$  terms. Since the stable manifolds are integrated backwards in time, the trajectories that intersect the asteroid surface

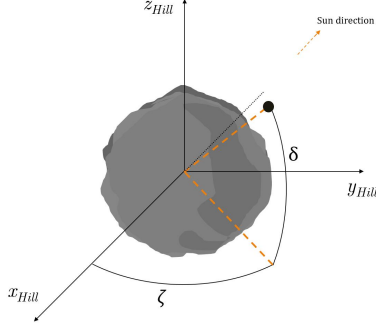


**Fig. 11 Spherical coordinates in the Hill frame.**

are in practice ejection trajectories - with a specific ejection location, velocity, and angle - that lead to the periodic orbits. For that reason, the term ejection conditions is often used to refer to the conditions of the stable manifolds at the intersection with the asteroid surface.

### A. Family *a*

A distribution of the ejection velocities for the trajectories that lead to family *a* can be seen in Figure 12, where Figure 12a shows the ejection velocities for any ejection angle and Figure 12b shows the ejection velocities for  $\sigma \in [35^\circ, 50^\circ]$ . Note that, as expected, all velocities are smaller than the local escape velocity of  $v_{esc} = \sqrt{2\mu/r}$ , which is marked in the figures with a dashed red line. The ejection velocities for the different values of  $\beta$  approach a common maximum, close to 37.9 cm/s, for which the periodic orbits are closest to the asteroid.

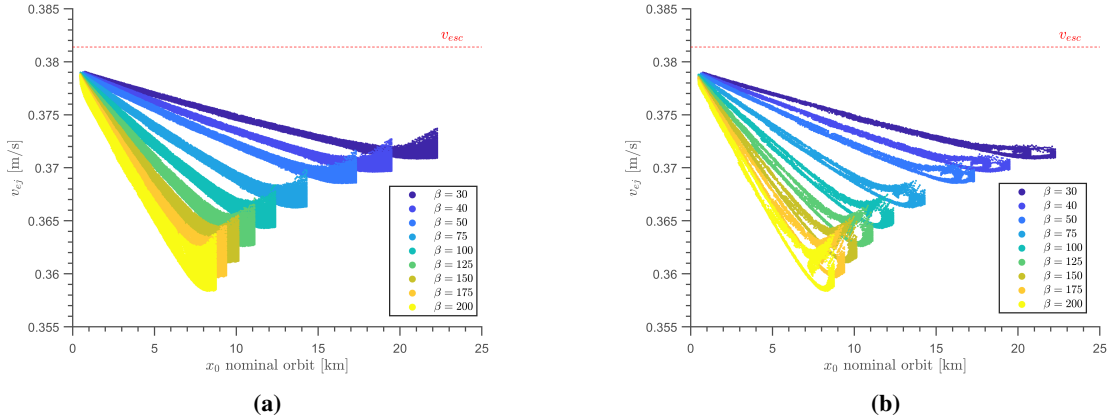


**Fig. 12 Ejection velocities for particles ejected along the stable manifolds of family *a* for different values of the SRP acceleration. (a) For any ejection angle; (b) for the expected ejection angles of  $\sigma \in [35^\circ, 50^\circ]$ .**

Figure 13 shows the distribution of the locations, along the asteroid's equator, where the stable manifolds of family *a* intersect the surface of the asteroid, i.e., the ejection locations. Figure 13a shows the distribution for all ejection angles while Figure 13b shows the distribution for  $\sigma \in [35^\circ, 50^\circ]$ . The length of the bars are cumulative for all  $\beta$ -values, where the bars are stacked vertically for the different values of  $\beta$  and the percentage shown on the vertical axis is calculated in the following way for each bin *i*

$$D^i = N_{ej}^i / N_{total} \times 100 \quad (12)$$

where  $N_{total}$  is the total number of stable manifold trajectories that intersect the surface of the asteroid for either all ejection angles or  $\sigma \in [35^\circ, 50^\circ]$  and  $N_{ej}^i$  is the number of manifold trajectories that intersect the asteroid at the right ascension defined by the  $i^{th}$  bin at either any ejection angle (Figure 13a) or at  $\sigma \in [35^\circ, 50^\circ]$  (Figure 13b). The sum of

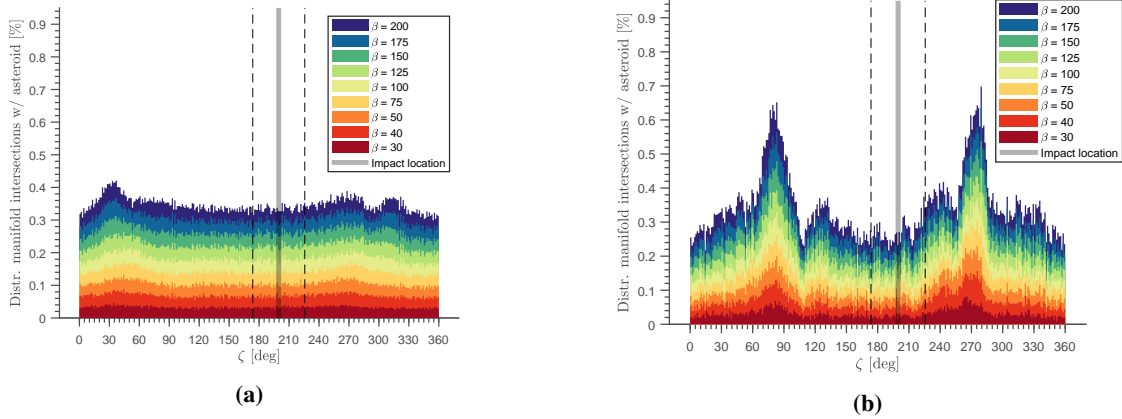


**Fig. 13** Distribution of the ejection locations for particles ejected along the stable manifolds of family  $a$  for different values of SRP acceleration. (a) For any ejection angle; (b) for ejection angles of  $\sigma \in [35^\circ, 50^\circ]$ .

all bars equates to 100%, for all  $\beta$ -values and each of the sub-figures. Note that we include the right ascension of the planned impact location of Hayabusa2's SCI (see Section V.D) as a vertical gray line, as well as the impact error radius, represented by dashed black lines and corresponding to approximately  $\Delta\zeta = 26^\circ$ .

When considering all ejection angles, the distribution of stable manifold intersections around the asteroid's equator is distributed approximately equally along  $\zeta$ , with a small peak around  $\zeta = 35^\circ$  and a small "valley" or minimum around  $\zeta = 0^\circ$ . However, when only considering ejection angles of  $\sigma \in [35^\circ, 50^\circ]$ , Figure 13 shows how local maxima develop around right ascensions of  $\zeta \approx 80^\circ$  and  $\zeta \approx 270^\circ$ . The reason for this is the decrease in manifold trajectories from the other right ascensions, due to the geometry of the manifolds and the considered constraint on the ejection angles. A few examples of the stable manifold trajectories that lead to orbits from the asteroid to family  $a$ , can be seen in Figure 14, where the trajectories with ejection angles between  $\sigma \in [35^\circ, 50^\circ]$  are shown in orange, and the others in gray and the escape trajectory of Hayabusa2 following the impact is also shown (see Section V.D). The manifold trajectories do indeed reach all right ascensions, but not always with an ejection angle between  $\sigma \in [35^\circ, 50^\circ]$ . Given that the locations  $\zeta \approx 80^\circ$  and  $\zeta \approx 270^\circ$  present more trajectories with an ejection angle between these limits, we see a higher relative concentration of ejection locations at these right ascensions.

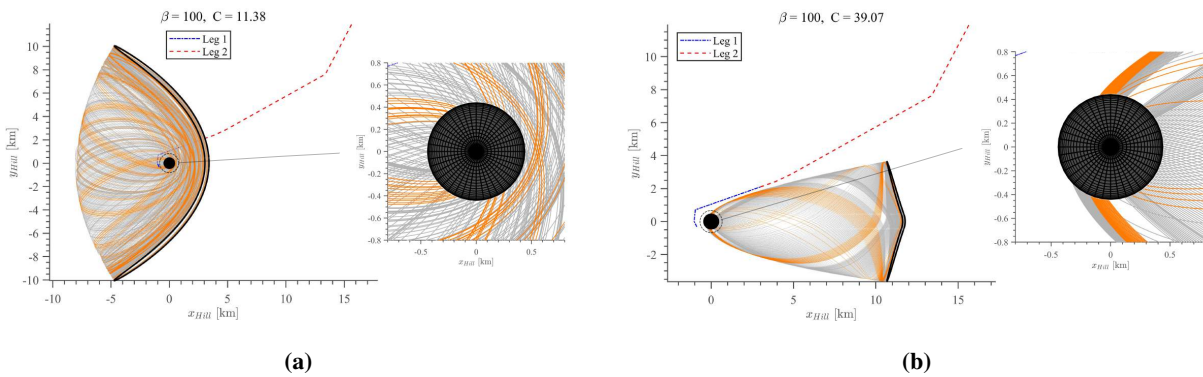


**Fig. 14** Examples of stable manifolds that lead to periodic orbits of family  $a$  and Hayabusa2's escape trajectory. The manifold trajectories with ejection angles between  $\sigma \in [35^\circ, 50^\circ]$  are shown in orange.

Table 3 displays the minimum, maximum, and mean times of flight,  $t_{flight}$  from the asteroid surface to the periodic orbits of family  $a$  of the particles with ejection angles  $\sigma \in [35^\circ, 50^\circ]$ , for different values of  $\beta$ . The minimum and maximum periods of the orbits in the family are also displayed. We note again that even though these orbits are unstable in the mathematical sense, a particle along said orbits would in principle not escape immediately after arriving at the

**Table 3** Times of flight along the stable manifolds of family  $a$ , between asteroid surface and periodic orbits, with ejection angles between  $\sigma \in [35^\circ, 50^\circ]$  and minimum and maximum periods in family for different values of  $\beta$ .

$\beta$	$\min\{t_{flight}\}$ [days]	$\max\{t_{flight}\}$ [days]	$mean\{t_{flight}\}$ [days]	$\min\{T\}$ [days]	$\max\{T\}$ [days]
30	60.3	149.9	79.3	21.3	38.4
50	41.9	148.5	55.6	14.4	26.4
100	25.5	143.1	32.8	8.6	15.9
150	19.1	135.4	24.2	6.4	11.7
200	15.5	122.7	19.4	5.2	9.5

orbit, but rather after a certain number of orbit revolutions. For instance, from Table 3, for  $\beta = 50$ , the minimum time of flight is 41.9 days; however, in addition to this, the particle will conduct a certain number of revolutions of the periodic orbit. If we consider a minimum of one revolution or period, this would still correspond to an extra 14.4 days, adding up to a minimum duration of 56.3 days during which the particle would remain close to the asteroid. Furthermore, note that the periods and times of flight decrease as the value of  $\beta$  increases, i.e., as the radius of the particles decreases. This can be explained by the equation for the Jacobi constant in Eq. (5); for the same position and value of  $C$ , an increase of  $\beta$  will cause the velocity to increase.

### B. Family $g'$

The velocity distribution of the particles ejected along the stable manifolds of family  $g'$  can be seen in Figure 15. The similarity to the velocity distribution of family  $a$  can be explained by the fact that both families exist close to each other in the family curve parameter space (see Figure 7). From the energy integral in Eq. (5), their velocities will therefore also be similar for similar ejection locations.

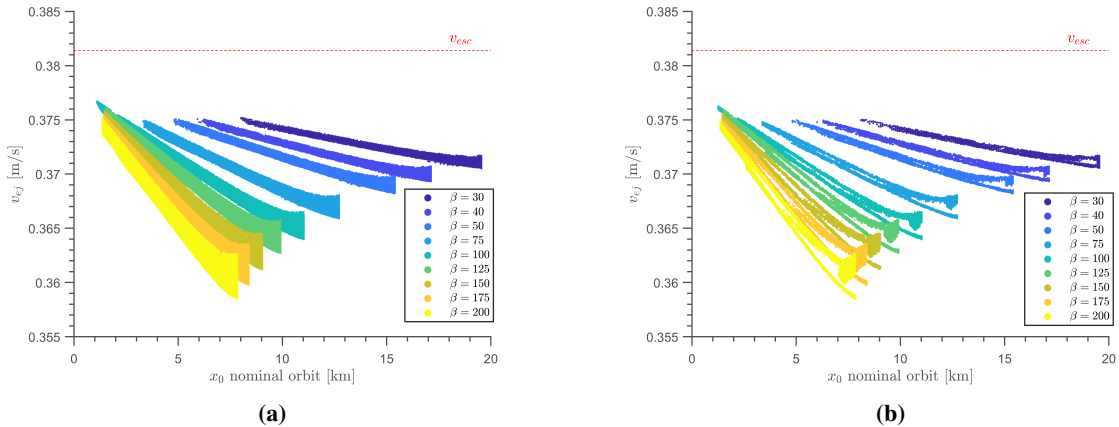


**Fig. 15** Ejection velocities for particles ejected along the stable manifolds of family  $g'$  for different values of SRP acceleration. (a) For any ejection angle; (b) for the expected ejection angles of  $\sigma \in [35^\circ, 50^\circ]$ .

The distribution of locations about the asteroid's equator where the stable manifolds of family  $g'$  intersect the asteroid can be seen in Figure 16. Both when considering all ejection angles (Figure 16a) and  $\sigma \in [35^\circ, 50^\circ]$  (Figure 16b), the distributions display minima and maxima. When considering all values for  $\sigma$ , we see a clear distribution with a minimum around  $\zeta \approx 90^\circ$  and a maximum between  $\zeta \in [295^\circ, 300^\circ]$ ; for the constrained ejection angles, we still see similar extrema, although the minimum becomes more profound and a second minimum appears between  $\zeta \in [260^\circ, 275^\circ]$ . This last minimum is very wide when considering smaller values of  $\beta$ : up to values of  $\beta = 50$ , the minimum extends over a range of  $\Delta\zeta = 30^\circ$ . The same occurs for the minimum around  $\zeta \approx 90^\circ$ . Note also the smaller peaks at  $\zeta \approx 165^\circ, 230^\circ$  and slight valley around  $\zeta \approx 195^\circ$  and when approaching  $\zeta = 360^\circ$ .

The *minima* for this distribution match very closely with the *maxima* found in the distribution of family  $a$  (see Figure

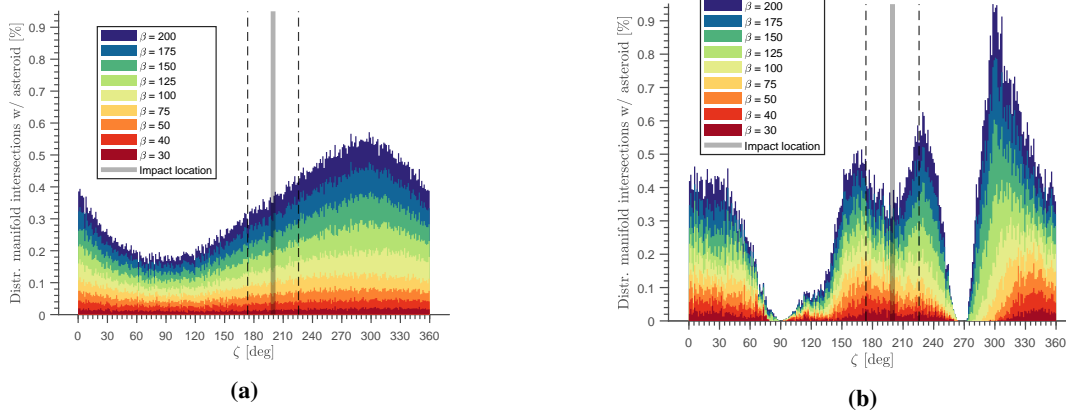


**Fig. 16** Distribution of the ejection locations for particles ejected along the stable manifolds of family  $g'$  for different values of SRP acceleration. (a) For any ejection angle; (b) for ejection angles of  $\sigma \in [35^\circ, 50^\circ]$ .

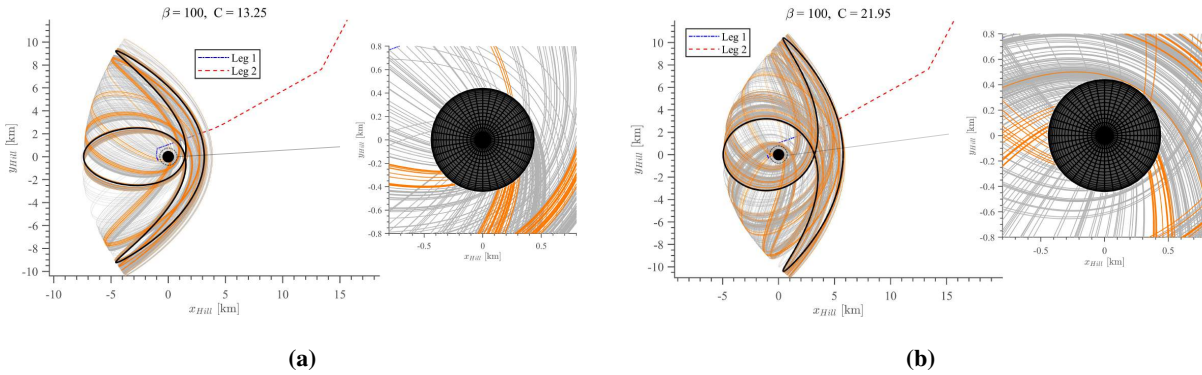


**Fig. 17** Examples of stable manifolds that lead to periodic orbits of family  $g'$  and Hayabusa2's escape trajectory. The manifold trajectories with ejection angles between  $\sigma \in [35^\circ, 50^\circ]$  are shown in orange.

13b). While for family  $g'$  it would make sense to choose an impact location with  $\zeta$  close to the  $y$ -axis, i.e.,  $\zeta = 270^\circ$ , family  $a$  shows a high concentration of manifold intersections for those right ascensions. Taking into account the fact that the distribution for family  $a$  does not vary significantly outside the regions where the maxima are located, for future events, choosing an impact location that minimizes the chances of ejecta getting captured into orbits of family  $g'$  is recommended, as long as that location is situated outside the maxima of family  $a$ , i.e., outside locations about  $\zeta \approx 80^\circ$  and  $\zeta \approx 270^\circ$ . For this reason, and taking into account a possible impact angle error, if impacting on the equator, an impact location around  $\zeta = 130^\circ$  is recommended, so as to minimize the chances of ejecta getting captured into either orbit family.

The distributions of the ejection locations for family  $g'$  seen in Figure 16 can be explained by the geometry of its stable manifolds and the effect of the angle restriction. The stable manifolds seldom intersect the asteroid at right ascensions of  $\zeta = 90^\circ$  and due to the geometry of the trajectories, the ejection angles of said trajectories are rarely within the specified limits. The lack of trajectories within the specified ejection angles is also why we see the minimum between  $\zeta \in [260^\circ, 275^\circ]$ . The maximum for  $\zeta \in [295^\circ, 300^\circ]$  follows the reciprocal reasoning: the geometry of the orbits and their stable manifolds allow for a large number of trajectories to reach those right ascensions, which have, in general,  $\sigma$  within the specified limits. Figure 17 shows examples of some of these trajectories.

Finally, Table 4 displays the minimum, maximum, and mean times of flight of the trajectories with ejection angles  $\sigma \in [35^\circ, 50^\circ]$  moving from asteroid surface to the periodic orbits of family  $g'$ , for the different values of  $\beta$ . The minimum times of flight range between 16.1 days for the smallest sized particles considered (millimeter size), and 61 days for the largest (centimeter size), which exclude the minimum orbit periods of 7 and 32 days, respectively. Note that

**Table 4** Times of flight along the stable manifolds of family  $g'$ , between asteroid surface and periodic orbits, with ejection angles between  $\sigma \in [35^\circ, 50^\circ]$  and minimum and maximum periods in family for different values of  $\beta$ .

$\beta$	$\min\{t_{flight}\}$ [days]	$\max\{t_{flight}\}$ [days]	$mean\{t_{flight}\}$ [days]	$\min\{T\}$ [days]	$\max\{T\}$ [days]
30	61.0	150.0	110.7	32.0	38.5
50	44.2	150.0	89.4	21.0	26.6
100	26.8	150.0	69.0	11.6	16.0
150	19.9	141.9	49.2	8.7	11.8
200	16.1	148.1	35.0	7.0	9.6

even for the smallest particles the maximum time of flight equates to 148.1 days.

### C. Terminator family

Figure 18 displays the ejection velocities into the stable manifolds of the terminator orbit family as a function of the initial  $x$ -coordinate,  $x_0$ , of the nominal orbit for all ejection angles (Figure 18a) and for  $\sigma \in [35^\circ, 50^\circ]$  (Figure 18b), the ejection velocities as a function of the ejection angle (Figure 18c), and the sections of the family curve whose stable manifolds intersect the asteroid (Figure 18d). Figure 18c shows how the minimal velocities are achieved for  $\sigma \in [40^\circ, 55^\circ]$  and the largest velocities comprise of near vertical ejections. Contrary to families  $a$  and  $g'$ , only part of the orbits of the family generate manifolds that intersect the asteroid surface: Figure 18d shows how only the stable manifolds from the orbits situated in the regions close to the equilibrium point intersect the asteroid. For the other orbits in the family, the stable manifolds approach the asteroid but never intersect its surface. They simply remain in a quasi-terminator orbit that is situated closer to the asteroid than the original nominal orbit.

Another observation regarding the geometry of the trajectories can be inferred from Figures 18a, 18b, and 18d. Note how the largest ejection velocities in Figure 18a correspond to periodic orbits furthest from the asteroid, i.e., the closest to the equilibrium point. This peak in ejection velocity can also be seen in Figure 18c for  $\sigma \approx 0^\circ$ . This means that the stable manifolds from the terminator orbits closest to the  $L_2$  equilibrium point will depart from the asteroid at the largest velocities and at near vertical trajectories with respect to the local vertical. This also implies that trajectories leading to orbits situated very close to the equilibrium point will likely not be followed by particles ejected from the asteroid surface, due to the ejection angle constraint.

In Figures 20 and 21, distribution maps of the ejection locations are shown. The color-map and percentages are calculated similarly to Eq. (12), although the distribution is cumulative, i.e., it is summed over all values of  $\beta$

$$D^i = \frac{\sum_{\beta} N_{ej}^i}{\sum_{\beta} N_{total}} \times 100 \quad (13)$$

Once again, for comparison purposes, the nominal impact point and the error radius for three standard deviations (see Section V.D) are displayed and plotted in red in Figures 20 and 21.

We define the subsolar and anti-subsolar points, which are placed on the intersection between the Sun-asteroid line and the asteroid surface on the Sun side and the night side of the asteroid, respectively. Analyzing Figure 20, we see that even when considering all ejection angles, certain locations on the asteroid are never intersected by stable manifold trajectories of the terminator family. These occur around the subsolar ( $\zeta = 180^\circ$ ) and anti-subsolar ( $\zeta = 0^\circ$ ) points, although the region on the Sun side is significantly larger. Moreover, on the night side of the asteroid, we see that this region is surrounded by locations with high concentrations of stable manifold intersections. These high-concentration regions originate in their majority from the manifolds of the orbits closest to the  $L_2$  point, which, as seen in Figure 19, mainly intersect the asteroid on the night side and around the anti-subsolar point. As the value of  $\beta$  increases and as we approach the  $L_2$  point, the manifolds tend to follow the path of the stable manifolds of the equilibrium point (see Figure 10), which always intersects the asteroid on the night side for sufficiently large values of  $\beta$ , as seen in Figure 19a. When we only consider  $\sigma \in [35^\circ, 50^\circ]$  (see Figure 21), we see how a well-defined band forms close to the  $yz$ -plane; no manifolds intersect with the asteroid surface outside this band when constraining  $\sigma$ . It is interesting to note that the maximum concentration of intersections occurs near the equator and for  $\zeta \in [70^\circ, 90^\circ]$  and  $\zeta \in [270^\circ, 290^\circ]$ , which are also regions where the manifold intersection distributions of families  $a$  and  $g'$  display maxima. Because

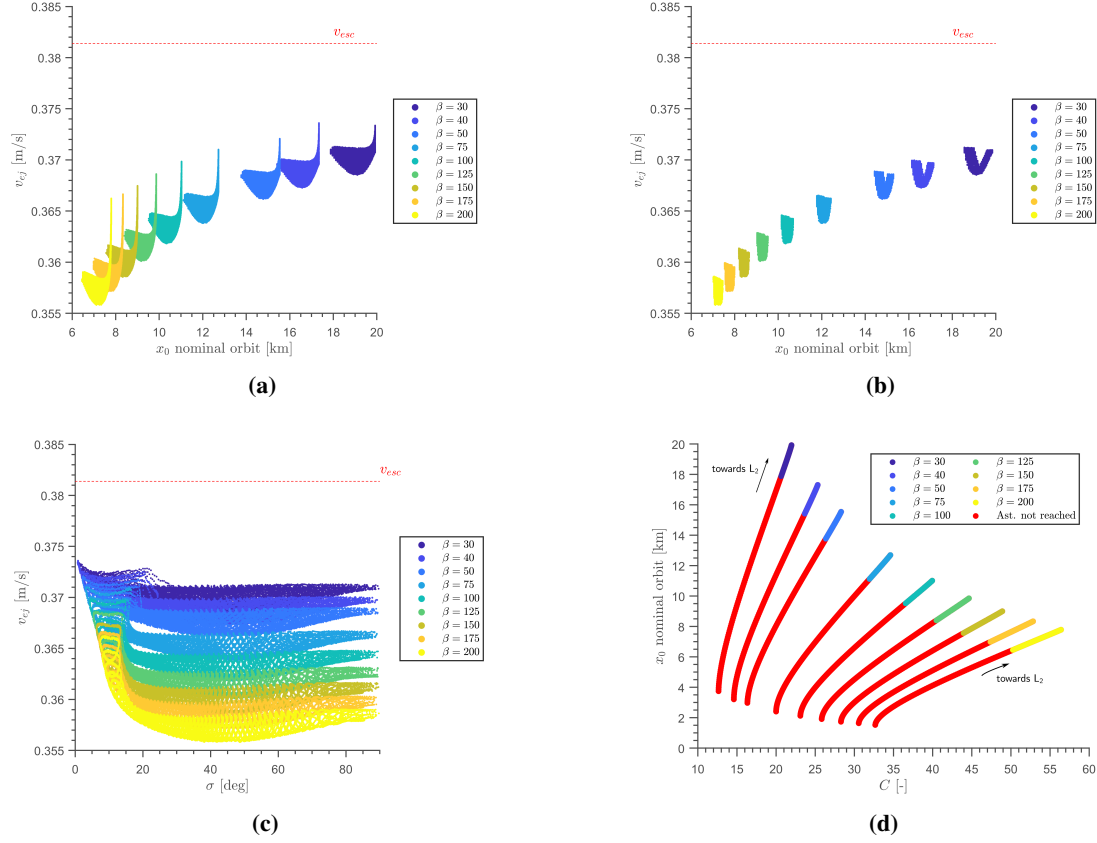


**Fig. 18** (a) Ejection velocities for particles ejected along the stable manifolds of the terminator family for different values of the SRP acceleration for any ejection angle; (b) for ejection angles of  $\sigma \in [35^\circ, 50^\circ]$ . (c) Ejection velocity as a function of ejection angle  $\sigma$ . (d) Sections of terminator orbit family for which at least one stable manifold trajectory intersects the asteroid for different values of SRP acceleration.

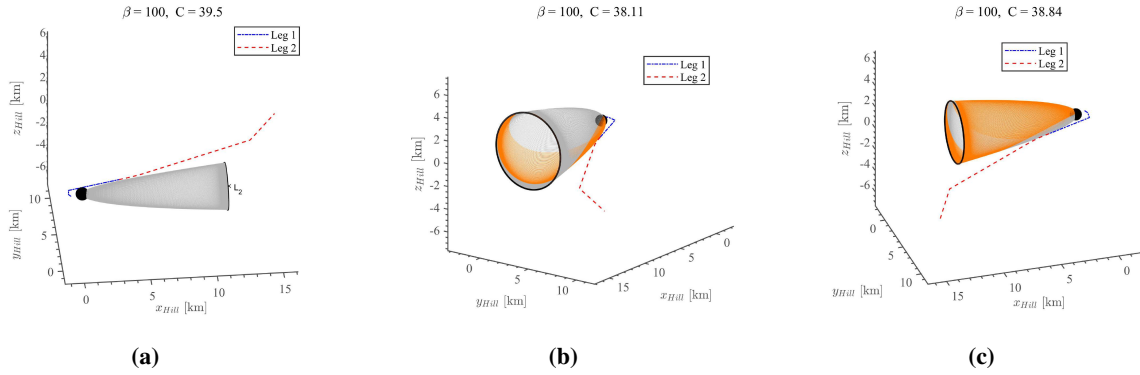


**Fig. 19** Examples of stable manifolds that lead to periodic orbits of the terminator family and Hayabusa2's escape trajectory. The manifold trajectories with ejection angles between  $\sigma \in [35^\circ, 50^\circ]$  are shown in orange.

the trajectories intersecting those regions have ejection angles outside the defined range, the imposed angle constraint forbids the existence of manifold trajectories in the regions outside the aforementioned band. Figures 20 and 21 show that the ejection angles of the stable manifolds do indeed follow a specific pattern with respect to the ejection location.

Finally, Table 5 provides information regarding the times of flight for the stable manifolds of the terminator family

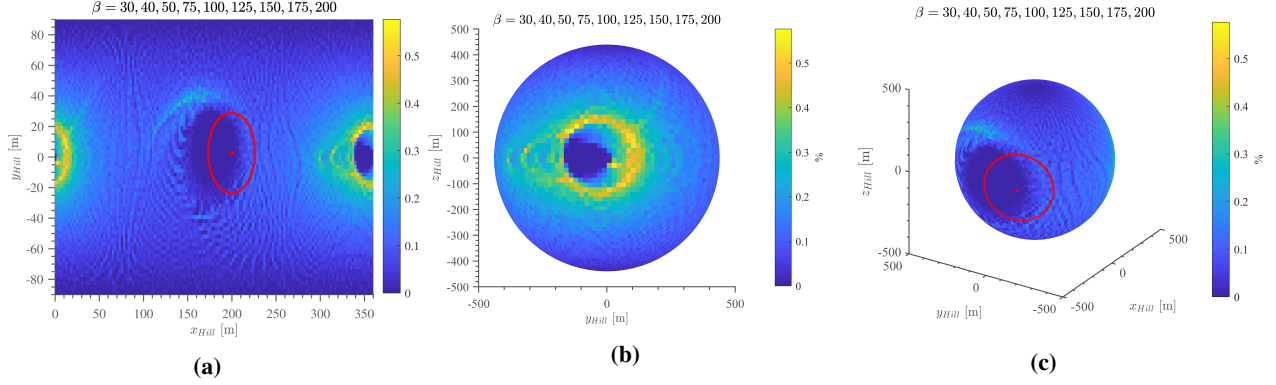


**Fig. 20** Cumulative distribution maps of the ejection locations for particles ejected along the stable manifolds of the terminator family when considering any ejection angle.

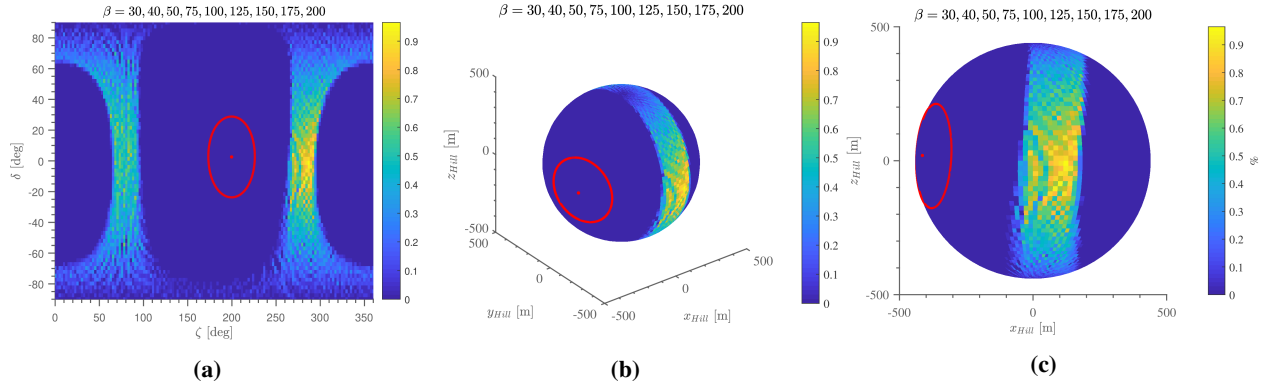


**Fig. 21** Cumulative distribution maps of the ejection locations for particles ejected along the stable manifolds of the terminator family for  $\sigma \in [35^\circ, 50^\circ]$ .

**Table 5** Times of flight along the stable manifolds of terminator family, between asteroid surface and periodic orbits, with ejection angles between  $\sigma \in [35^\circ, 50^\circ]$  and minimum and maximum periods in family for different values of  $\beta$ .

$\beta$	$\min\{t_{flight}\}$ [days]	$\max\{t_{flight}\}$ [days]	$mean\{t_{flight}\}$ [days]	$\min\{T\}$ [days]	$\max\{T\}$ [days]
30	59.1	123.9	61.3	35.3	36.2
50	41.0	41.1	41.0	24.2	24.8
100	24.8	24.8	24.8	14.4	14.7
150	18.4	18.5	18.4	10.5	10.8
200	14.9	15.0	15.0	8.5	8.7

with  $\sigma \in [35^\circ, 50^\circ]$ , as well as the minimum and maximum periods of the orbits in the family for the different values of  $\beta$ . Note that the times of flight and periods are smaller for the terminator family than for families  $a$  and  $g$ . Moreover, note that for  $\beta \leq 50$  ( $R \leq 3.1$  cm), the times of flight display very small variations with respect to the mean value. Nonetheless, for  $\beta = 30$  ( $R = 5.2$  cm), a particle ejected along the stable manifolds of a terminator orbit could remain about the asteroid for 160.1 days ( $123.9 + 36.2$ ). For particles with  $\beta = 150$  ( $R = 1.0$  cm) this time drops to 29.3 days ( $18.5 + 10.8$ ).

## D. Hayabusa2

In April 2019, Hayabusa2 successfully carried out its SCI operation, with no harm to the spacecraft [44]. After the SCI was separated, Hayabusa2 began the first leg of its escape trajectory, hiding behind the asteroid in order to shield itself from the debris generated by the charge detonation. Figure 22 shows the three legs of the escape trajectory, which took place throughout the two weeks following the impact operation, and where the spacecraft proceeded to move further away from the asteroid and then return to its nominal "Home Position", on the Sun side of asteroid [41]. Legs 1 and 2 are also shown before in Figures 14, 17, and 19. The planned impact location for the SCI was on the Sun side of the asteroid, as shown in Figure 23, slightly above the equator in the positive direction of the  $z$ -axis. Additionally, Figure 23 includes also the error radius of the impact location, corresponding to the three standard deviations and approximately a 200 m radius ( $\Delta\zeta = 26^\circ$ ).

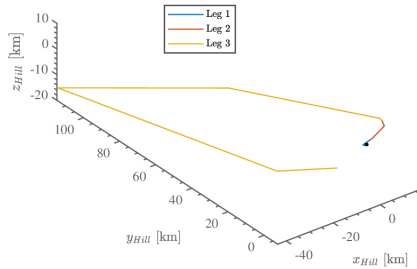


**Fig. 22** Hayabusa2's escape trajectory [41].

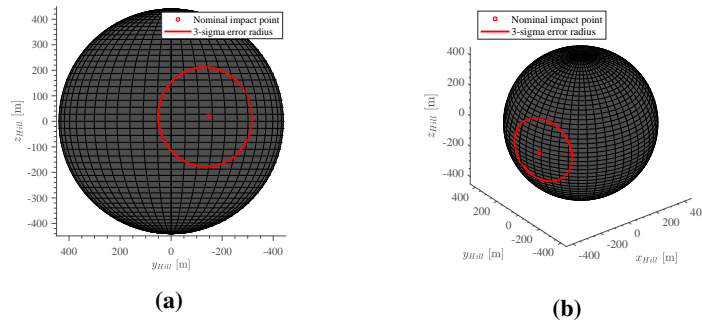


**Fig. 23** Nominal impact location and error radius given by three standard deviations [41].

After the SCI operation, the Hayabusa2 spacecraft returned to its nominal position - around 20 km from the asteroid in the direction of the Earth [1]. The actual impact location was relatively close to that planned, in a region identified in this paper as ideal to minimize temporary capture of particles. From the results obtained, an ideal impact region would be on the Sun side of the asteroid, for medium latitudes or outside the equator region. The actual impact location, which was approximately two degrees north of the planned location [44], was then contained within this region. Up to date, no temporarily captured particles have been detected.

Analyzing the SCI operation, the escape trajectory of the spacecraft consisted of a good safety measure for the first period after the impact event. The spacecraft was also below the  $xy$ -plane (in the negative  $z$  direction of the Hill frame), which ensured no collision with a planar trajectory could occur. Furthermore, as mentioned, following the ballistic impact, high-velocity material is ejected from the surface. For this reason, it makes sense to place the impact location and the spacecraft on opposite sides of the asteroid during impact, therefore making sure that the spacecraft is not hit by the escaping high-velocity particles. This measure was implemented in the SCI operation, as seen in Figures 22 and 23. Additionally, note that although some of the manifold trajectories shown seem to intersect the escape trajectory of the spacecraft (Figures 14, 17, and 19), they would do so after Hayabusa2 had passed through those regions.

An important outcome from the presented results is that, if ejected into the stable manifold trajectories of periodic orbits at the correct velocity, ejecta particles could remain about the asteroid for very long periods of time. The duration of this temporary capture varies depending on the orbit family and the size of the particle (which translates into different values of  $\beta$ ). The smallest particles will on average remain about the asteroid for shorter periods of time, but can reach values ranging from 21 days to 158 days for particles with a radius of 7.8 mm, and from 81 days to 189 days for particles with a radius of 5.2 cm. These are conservative estimates because the particles are assumed to remain in the periodic orbit for only one orbital revolution. This means that the choice in impact location is of significant importance when attempting to minimize temporary capture of ejecta particles.

A final remark concerning the safety of a future impact cratering mission is made, with respect to the trajectories that ejecta particles can take after their temporary capture. From Figure 9, we see that for a particle to escape, the ZVCs must be open at the  $L_2$  point. However, because the  $L_2$  point is always on the night side of the asteroid and because the ZVCs do not open on the Sun side of the asteroid when considering SRP (only for high-velocity particles, which is not the case of captured ejecta), these particles will not escape into the Sun direction. For this reason, after being temporarily captured, the ejecta particles will either escape the asteroid's vicinity in the anti-solar direction or re-impact

on its surface. Keeping the spacecraft on the Sun side of the asteroid when returning to its vicinity, which, as seen in Figure 22, was the case for Hayabusa2, decreases the possibility of ejecta particles colliding with the spacecraft.

## VI. Conclusion

This paper has analyzed the possibility of ejecta particles getting temporarily captured into periodic orbits about an asteroid following an artificial impact on its surface. Three families of periodic orbits – families  $a$  and  $g'$  from the traditional Hill Problem and the family of southern halo orbits or terminator orbits – have been studied in the dynamical framework of the perturbed Augmented Hill Problem (AHP), which includes the effects of solar radiation pressure (SRP), eclipses, and the oblateness of the asteroid, represented by the  $J_{20}$  and  $J_{40}$  terms of its spherical harmonics gravity potential expansion. Within this model, it was shown that centimeter- to millimeter-sized particles could remain trapped about the asteroid for long periods of time as a consequence of a ballistic impact event, if ejected along the stable manifolds of these periodic orbits. These periods were shown to range from 21 to 189 days in conservative considerations, a value that would limit and possibly jeopardize a mission's operations. On average, the ejecta particles with smaller radii were shown to remain captured for shorter periods of time than those with larger radii. The conditions for temporary orbital capture into periodic orbits were also investigated, specifically the ejection locations of these particles. We defined the subsolar and anti-subsolar points as the intersection of the Sun-asteroid line with the asteroid surface on the Sun and night sides of the asteroid, respectively. Using this, it was found that a ballistic impact on the equator of the asteroid, approximately  $\pm 80^\circ$  from the anti-subsolar point, would lead to the largest numbers of ejecta particles being captured into the three considered periodic orbit families. Specifically, the location at  $-80^\circ$  from the anti-subsolar direction (where the positive direction is given by the angular momentum vector of the asteroid's orbit about the Sun), was shown to be near the maxima for all three families. On the contrary, it was shown that an impact location on the Sun side of the asteroid, not intersecting the equator, would not cause any particles to be captured into the aforementioned families of periodic orbits. For this reason, and considering an impact error radius, the best impact location for an artificial cratering event was found to be on the Sun side of the asteroid, at medium latitudes. Additionally, it was found that the ranges of ejection velocities that cause particles to be captured into the three families of periodic orbits were very similar for both different sized particles and different families, ranging between 0.355 and 0.380 m/s for the case of asteroid Ryugu. Furthermore, besides verifying the fact that, in general, solar radiation pressure cannot be neglected when studying the dynamical environment around small bodies (both for ejecta particles and spacecraft), other theoretical outcomes were obtained in this study. Firstly, it was shown that the stable manifold of the only equilibrium point of the system, which is situated on the night side of the asteroid, intersects the asteroid surface and tends to travel along the Sun-asteroid line for sufficiently large values of solar radiation pressure acceleration (the same will occur for the unstable manifold, although it was not analyzed in this work). Secondly, the effect of the solar radiation pressure on the manifolds of the families of periodic orbits was analyzed. It was found that their geometry changes significantly and that in the case of libration point orbits (as the terminator and  $a$  families) the shape and direction of their manifolds tend to follow the manifolds of the libration point for increasing values of solar radiation pressure acceleration. Finally, due to the large relative values of solar radiation pressure acceleration, it was concluded that the effect of eclipses should not be neglected. In fact, it was demonstrated that the stability of periodic orbits that pass through eclipse regions changes significantly when including the effect of eclipses. This last observation has not only implications to the study of particle dynamics, but also to the design of space missions.

## References

- [1] Tsuda, Y., Yoshikawa, M., Abe, M., Minamino, H., and Nakazawa, S., "System Design of the Hayabusa 2 - Asteroid Sample Return Mission to 1999 JU3," *Acta Astronautica*, Vol. 91, 2013, pp. 356–362. doi:10.1016/j.actaastro.2013.06.028.
- [2] Galvez, A., Carnelli, I., Michel, P., Cheng, A. F., Reed, C., Ulamec, S., Biele, J., Abell, P. A., and Landis, P., "AIDA: The Asteroid Impact & Deflection Assessment Mission," *European and Planetary Science 2013, Congress Abstracts*, Vol. 8, 2013, p. Abstract 1043.
- [3] Snodgrass, C., Tubiana, C., Vincent, J. B., Sierks, H., Hviid, S., Moissl, R., ..., and Wenzel, K. P., "A Collision in 2009 as the Origin of the Debris Trail of Asteroid P/2010 A2," *Nature*, Vol. 467, No. 7317, 2010, pp. 814–816. doi:10.1038/nature09453.
- [4] Scheeres, D. J., and Mazary, F., "Spacecraft Dynamics in the Vicinity of a Comet," *Journal of the Astronautical Sciences*, Vol. 50(1), No. January, 2002, pp. 35–52.
- [5] Matakuma, T., "On the Periodic Orbits in Hill's Case," *Proc. Imp. Acad. Tokyo*, Vol. 6, No. 1, 1930, pp. 6–8.
- [6] Henon, M., "Numerical Exploration of the Restricted Problem. V. Hill's Case: Periodic Orbits and Their Stability," *Astronomy and Astrophysics*, Vol. 1, No. 2, 1969, pp. 223–238.
- [7] Scheeres, D. J., Durda, D. D., and Geissler, P. E., "The Fate of Asteroid Ejecta," *Asteroids III*, 2002, pp. 527–544.
- [8] Scheeres, D. J., *Orbital Motion in Strongly Perturbed Environments - Applications to Asteroid, Comet and Planetary Satellite*

- Orbiters*, Springer-Verlag Berlin Heidelberg, 2012. doi:10.1007/978-3-642-03256-1.
- [9] Papadakis, K. E., “The Planar Photogravitational Hill Problem,” *International Journal of Bifurcation and Chaos*, Vol. 16, No. 6, 2006, pp. 1809–1821.
- [10] Heiligers, J., and Scheeres, D. J., “Solar Sail Orbital Motion About Asteroids and Binary Asteroid Systems,” *Journal of Guidance, Control, and Dynamics*, No. April, 2018, pp. 1–18. doi:10.2514/1.G003235.
- [11] Basiana Farrés, A., Soldini, S., and Tsuda, Y., “JAXA’s Trojan Asteroids Mission: Trajectory Design of the Solar Power Sail and its Lander,” *4th International Symposium on Solar Sailing*, 2017, pp. 1–7.
- [12] Broschart, S. B., and Villac, B. F., “Identification of Non-Chaotic Terminator Orbits near 6489 Golevka,” *Advances in the Astronautical Sciences*, Vol. 134, No. February 2009, 2009, pp. 861–880. doi:10.13140/2.1.1246.8484.
- [13] Scheeres, D. J., “Satellite Dynamics about Asteroids,” *Advances in the Astronautical Sciences*, Vol. 87, No. 1, 1994, pp. 275–292.
- [14] Dankowicz, H., “Some Special Orbits in the Two-Body Problem with Radiation Pressure,” *Celestial Mechanics & Dynamical Astronomy*, Vol. 58, No. 4, 1994, pp. 353–370. doi:10.1007/BF00692010.
- [15] Scheeres, D. J., Williams, B. G., and Miller, J. K., “Evaluation of the Dynamic Environment of an Asteroid: Applications to 433 Eros,” *Advances in the Astronautical Sciences*, Vol. 102 II, No. 3, 1999, pp. 835–848. doi:10.2514/2.4552.
- [16] Howell, K. C., “Three-Dimensional, Periodic, ‘Halo’ Orbits,” *Celestial Mechanics*, Vol. 32, 1984, pp. 53–71.
- [17] Broschart, S. B., Lantoine, G., and Grebow, D. J., “Quasi-Terminator Orbits near Primitive Bodies,” *Celestial Mechanics and Dynamical Astronomy*, Vol. 120, No. 2, 2014, pp. 195–215. doi:10.1007/s10569-014-9574-3.
- [18] Giancotti, M., Campagnola, S., Tsuda, Y., and Kawaguchi, J., “Families of Periodic Orbits in Hill’s Problem with Solar Radiation Pressure: Application to Hayabusa 2,” *Celestial Mechanics and Dynamical Astronomy*, Vol. 120, No. 3, 2014, pp. 269–286. doi:10.1007/s10569-014-9564-5.
- [19] García Yarnoz, D., and McInnes, C. R., “On the a and g Families of Orbits in the Hill Problem with Solar Radiation Pressure and their Application to Asteroid Orbiters,” *Celestial Mechanics & Dynamical Astronomy*, Vol. 121, 2015, pp. 365–384. doi:10.1007/s10569-015-9604-9.
- [20] Scheeres, D. J., Ostro, S. J., Hudson, R. S., and Werner, R. A., “Orbits close to Asteroid 4769 Castalia,” *Icarus*, Vol. 121, No. 1, 1996, pp. 67–87. doi:10.1006/icar.1996.0072.
- [21] Soldini, S., and Tsuda, Y., “Assessing the Hazard Posed by Ryugu Ejecta Dynamics on Hayabusa2 Spacecraft,” *26th International Symposium of Space Flight Dynamics*, 2017, pp. 1–11.
- [22] Hamilton, D. P., and Krivov, A. V., “Circumplanetary Dust Dynamics: Effects of Solar Gravity, Radiation Pressure, Planetary Oblateness, and Electromagnetism,” *Icarus*, Vol. 123, No. 2, 1996, pp. 503–523. doi:10.1006/icar.1996.0175.
- [23] Szebehely, V., *Theory of Orbits - The Restricted Problem of Three Bodies*, Academic Press, 1967.
- [24] McInnes, C., *Solar Sailing: Technology, Dynamics and Mission Applications*, Springer-Verlag Berlin Heidelberg, 1999. doi:10.2514/2.4604.
- [25] Mueller, T. G., Durech, J., Hasegawa, S., Abe, M., Kawakami, K., ..., and Kasuga, TNagayama, S., “Thermo-Physical Properties of 162173 (1999 JU3), a Potential Flyby and Rendezvous Target for Interplanetary Missions,” *Astronomy and Astrophysics*, Vol. 525, No. A145, 2011, pp. 1–6. doi:10.1051/0004-6361/201015599.
- [26] Han, J., and Moraga, C., “The Influence of the Sigmoid Function Parameters on the Speed of Backpropagation Learning,” *From Natural to Artificial Neural Computation*, edited by J. Mira and F. Sandoval, Springer Berlin Heidelberg, 1995, pp. 195–201.
- [27] Rossi, A., Marzari, F., and Farinella, P., “Orbital Evolution around Irregular Bodies,” *Earth Planets Space*, Vol. 51, 1999, pp. 1173–1180.
- [28] Vallado, A. D., *Fundamentals of Astrodynamics and Applications*, Microcosm Press/Springer, 1997. doi:10.2514/2.4291.
- [29] Villac, B. F., and Scheeres, D. J., “Escaping Trajectories in the Hill Three-Body Problem and Applications,” *Journal of Guidance, Control, and Dynamics*, Vol. 26, No. 2, 2003, pp. 224–232. doi:10.2514/2.5062.
- [30] Parker, J. S., and Anderson, R. L., *Low-Energy Lunar Trajectory Design*, Jet Propulsion Laboratory, Pasadena, California, 2013. doi:10.1002/9781118855065.
- [31] Muñoz-Almaraz, F. J., Freire, E., Galán, J., Doedel, E., and Vanderbauwhede, A., “Continuation of Periodic Orbits in Conservative and Hamiltonian Systems,” *Physica D*, Vol. 181, 2003, pp. 1–38. doi:10.1016/S0167-2789(03)00097-6.
- [32] Montenbruck, O., and Eberhard, G., *Satellite Orbits - Models, Methods and Applications*, Springer-Verlag Berlin Heidelberg, 2000.
- [33] Scheeres, D. J., “Orbit Mechanics About Asteroids and Comets,” *Journal of Guidance, Control, and Dynamics*, Vol. 35, No. 3, 2012, pp. 987–997. doi:10.2514/1.57247.
- [34] Scheeres, D. J., and Marzari, F., “Temporary Orbital Capture of Ejecta from Comets and Asteroids: Application to the Deep Impact Experiment,” *Astronomy and Astrophysics*, Vol. 756, 2000, pp. 747–756.
- [35] Yu, Y., Michel, P., Schwartz, S. R., Naidu, S. P., and Benner, L. A., “Ejecta Cloud from the AIDA Space Project Kinetic Impact on the Secondary of a Binary asteroid: I. Mechanical Environment and Dynamical Model,” *Icarus*, Vol. 282, 2017, pp. 313–325. doi:10.1016/j.icarus.2016.09.008.
- [36] Melosh, H. J., *Impact Cratering - A Geologic Process*, Oxford University Press, 1989.
- [37] Cintala, M. J., Berthoud, L., and Horz, F., “Ejection-Velocity Distributions from Impacts into Coarse-Grained Sand,” *Meteoritics & Planetary Science*, Vol. 34, 1999, pp. 605–623.
- [38] Anderson, J. L. B., Schultz, P. H., and Heineck, J. T., “Asymmetry of Ejecta Flow during Oblique Impacts using Three-Dimensional Particle Image Velocimetry,” *Journal of Geophysical Research*, Vol. 108, No. E8, 2003, pp. 1–10. doi:10.1029/2003JE002075.
- [39] Gault, D. E., and Wedekind, J. A., “Experimental Studies of Oblique Impact,” *Proceedings of the 9th Lunar and Planetary Science Conference*, 1978, pp. 3843–3875.
- [40] Pierazzo, E., and Melosh, H. J., “Understanding Oblique Impacts from Experiments, Observations, and Modeling,” *Annual Review of Earth Planetary Science*, Vol. 67, 2000, pp. 28–141.
- [41] Saiki, T., Imamura, H., Arakawa, M., Wada, K., Takagi, Y., Hayakawa, M., Shirai, K., Yano, H., and Okamoto, C., “The Small

- Carry-on Impactor ( SCI ) and the Hayabusa2,” *Space Sci Rev*, 2017, pp. 165–186. doi:10.1007/s11214-016-0297-5.
- [42] Melosh, H. J., “Impact Ejection, Spallation, and the Origin of Meteorites,” *Icarus*, Vol. 59, 1984, pp. 234–260.
- [43] Koon, W. S., Lo, M. W., Marsden, J. E., and Ross, S. D., *Dynamical Systems, the Three-Body Problem and Space Mission Design*, 2011.
- [44] JAXA Hayabusa2 Project, “Asteroid explorer, Hayabusa2, reporter briefing - May 9th,” Tech. rep., 2019.